N90-21083

CSI Sensing and Control:
Analytical and Experimental Results

J. L. Junkins, T. C. Pollock, and
Z. H. Rahman
Texas A&M University
College Station, Texas

C-5

Preface

We present here some of our recent work on structural identification and large-angle maneuvers with vibration suppression. Our recent work has sought to balance structural and controls analysis activities by involving the analysts directly in the validation and experimental aspects of the research. We have successfully implemented some new sensing, actuation, system identification, and control concepts. An overview of these results is given herein.

Acknowledgments

We distinguish between modal and model identification. In modal identification, we seek to extract the natural frequencies, damping factors, and mode shapes from (typically) a free decay response to impulsive initial conditions. In model identification, we seek the estimates of a particular set of physical parameters contained in our best available model of the structure, so that our computed (free or forced) response of the system is in best agreement with the measured response.

In our approach to model identification (see next page for roadmap figure), we utilize modal identification as a preprocessor. That is, we consider the $\{\omega\text{'s}, \xi\text{'s}, \text{ and } \phi\text{'s}\}$ determined from free vibration measurements as additional measurements to our model identification process wherein we seek to fit the measured input/output behavior by the frequency response from our model of the system. See reference 1 for details.

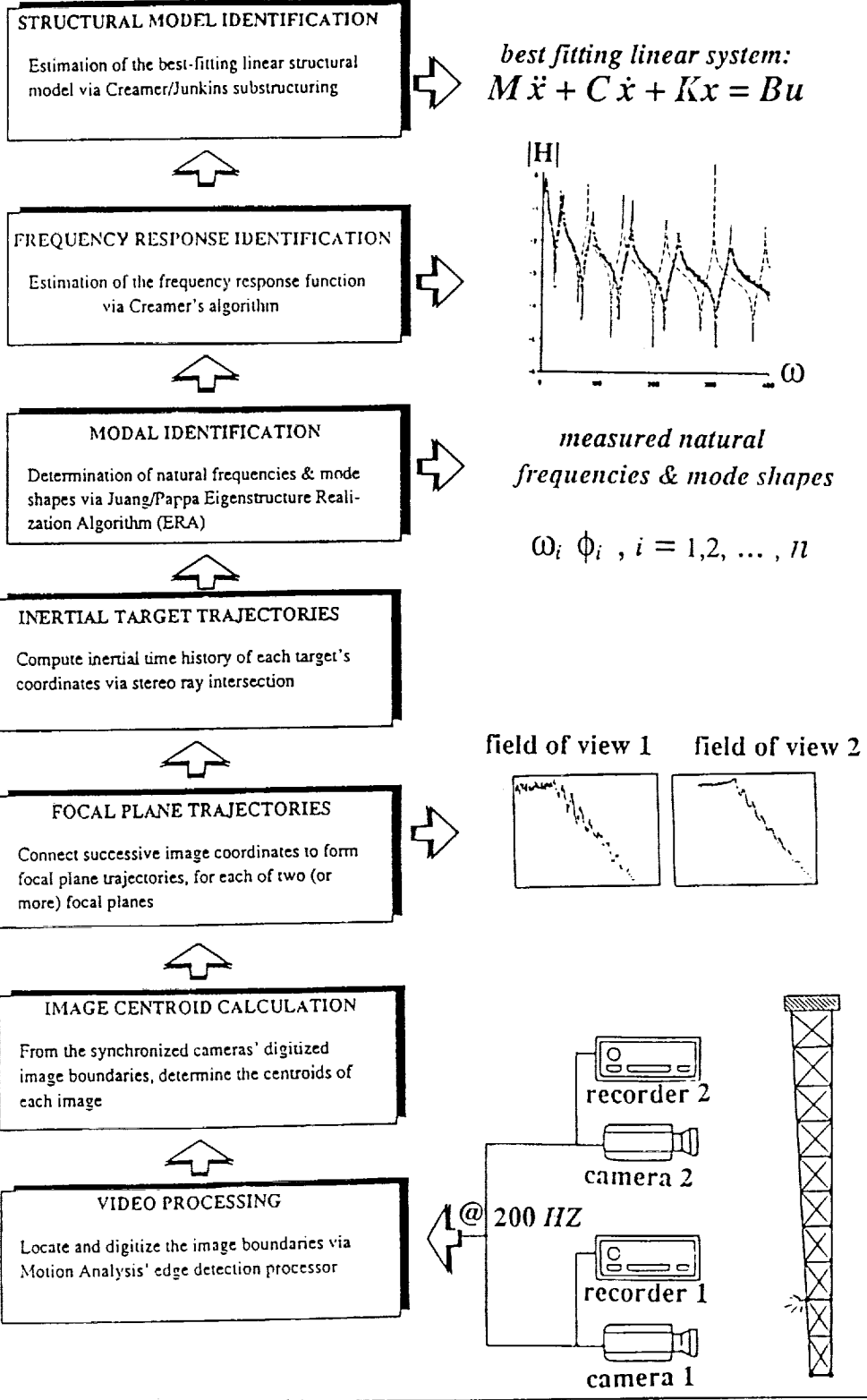# *OUTLINE*

- ## TAMU Flexible Grid Experiments

    Structural Identification
    Test Article, Sensors, and Actuators
    Stereo-Triangulation Deflection Measurements
    Measured Response Results
    Creamer/Junkins Method for System Identification
    Modeled, Measured, and Identified Frequencies & Mode Shapes

- ## Large Angle Maneuver Experiment

    Configuration Description and Dynamical Model
    Torque-Shaped, Near-Minimum-Time Maneuvers
    Liapunov-Stable Feedback Control
    Experimental Results

- ## Concluding Remarks
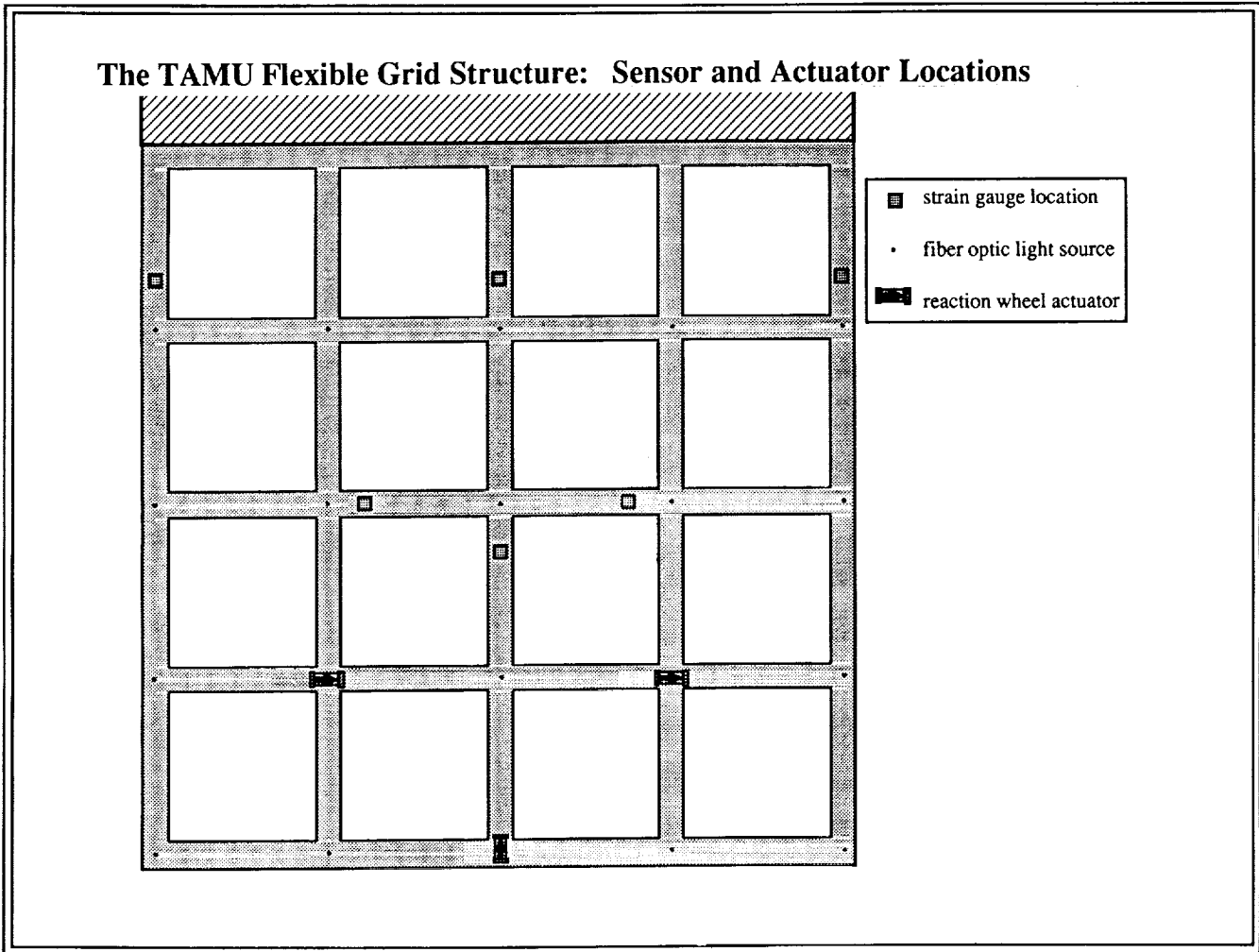
A Novel Approach to Structural Identification

STRUCTURAL MODEL IDENTIFICATION

Estimation of the best-fitting linear structural model via Creamer/Junkins substructuring

⇨ *best fitting linear system:*
$$M\ddot{x} + C\dot{x} + Kx = Bu$$

⇧

FREQUENCY RESPONSE IDENTIFICATION

Estimation of the frequency response function via Creamer's algorithm

⇨ |H| vs ω plot

⇧

MODAL IDENTIFICATION

Determination of natural frequencies & mode shapes via Juang/Pappa Eigenstructure Realization Algorithm (ERA)

⇨ *measured natural frequencies & mode shapes*

$$\omega_i \ \phi_i \ , \ i = 1, 2, \ldots , n$$

⇧

INERTIAL TARGET TRAJECTORIES

Compute inertial time history of each target's coordinates via stereo ray intersection

⇧

FOCAL PLANE TRAJECTORIES

Connect successive image coordinates to form focal plane trajectories, for each of two (or more) focal planes

⇨ field of view 1   field of view 2

⇧

IMAGE CENTROID CALCULATION

From the synchronized cameras' digitized image boundaries, determine the centroids of each image

recorder 2

camera 2

⇧

VIDEO PROCESSING

Locate and digitize the image boundaries via Motion Analysis' edge detection processor

⇦ @ 200 *HZ*

recorder 1

camera 1

This is a sketch of a 5 ft by 5 ft aluminum grid we've been using for a structural identification and vibration control experimental test article. The grid is cantilevered in the vertical plane. We cut this grid from a single sheet of aluminum, so it is jointless. However, a lap joint grid of identical geometry has been developed and is the subject of a similar experimental program by Alok Das et al. at AFAL.

Note that we have 20 optical targets on the grid. Presently these targets are actively illuminated by fiber optic light guides, but we have also successfully used passive targets made from reflective tape ("scotchlite" made by 3M). These optical targets are visible in two video cameras (200 or 60 frames per second); stereo triangulation of centroided image coordinates leads to measured inertial trajectories for each target. We also have six strain gauges mounted on the back of the grid at the stations shown, and we utilize three piezo-electric accelerometers that can be mounted at any three of the grid locations.

Excitation is provided by three grid-mounted reaction wheels (driven by Clifton Precision motors) with their torque axis in the plane of the grid in the directions shown (±20 oz-in. over the bandwidth from 0 to 40 Hz). We also utilize an impulse hammer to impart calibrated initial impulse excitation at any station.

The TAMU Flexible Grid Structure: Sensor and Actuator Locations

strain gauge location

fiber optic light source

reaction wheel actuator

We summarize the geometric equations governing triangulation of video camera imagery. With reference to the left figure, the image coordinates (x,y), measured in the positive focal plane of a single lens camera, are related (ref. 2) to the object space coordinates (X,Y,Z) of the imaged point, the camera's principal point (X_c, Y_c, Z_c), orientation angles (ϕ, θ, ψ), principal point offset (x_o, y_o), and focal length (f), by the colinearity equations

$$x = x_o - f\left[\frac{c_{11}(X-X_c)+c_{12}(Y-Y_c)+c_{13}(Z-Z_c)}{c_{31}(X-X_c)+c_{32}(Y-Y_c)+c_{33}(Z-Z_c)}\right] \equiv F(X,Y,Z;X_c,Y_c,Z_c;\phi,\theta,\psi;x_o,y_o,f)$$

$$y = y_o - f\left[\frac{c_{21}(X-X_c)+c_{22}(Y-Y_c)+c_{23}(Z-Z_c)}{c_{31}(X-X_c)+c_{32}(Y-Y_c)+c_{33}(Z-Z_c)}\right] \equiv G(X,Y,Z;X_c,Y_c,Z_c;\phi,\theta,\psi;x_o,y_o,f)$$

$$\begin{bmatrix} c_{11} & c_{12} & c_{13} \\ c_{21} & c_{22} & c_{23} \\ c_{31} & c_{32} & c_{33} \end{bmatrix} = \begin{bmatrix} 1 & 0 & 0 \\ 0 & \cos\psi & \sin\psi \\ 0 & -\sin\psi & \cos\psi \end{bmatrix} \begin{bmatrix} \cos\theta & 0 & -\sin\theta \\ 0 & 1 & 0 \\ \sin\theta & 0 & \cos\theta \end{bmatrix} \begin{bmatrix} \cos\phi & \sin\phi & 0 \\ -\sin\phi & \cos\phi & 0 \\ 0 & 0 & 1 \end{bmatrix}$$

$$(1)$$

We adopt a double subscript notation for eqs. (1) to denote the image coordinates of the ith point measured in the jth camera's image space as

$$x_{ij} = F(X_i, Y_i, Z_i; X_{c_j}, Y_{c_j}, Z_{c_j}; \phi_j, \theta_j, \psi_j; x_{o_j}, y_{o_j}, f_j)$$
$$y_{ij} = G(X_i, Y_i, Z_i; X_{c_j}, Y_{c_j}, Z_{c_j}; \phi_j, \theta_j, \psi_j; x_{o_j}, y_{o_j}, f_j), \quad j=1,2; \; i=1,2,\ldots,N$$

$$(2)$$

In the event that the camera position, orientation, and calibration constants are considered known, measurement of image coordinates of object space points at unknown locations, eqs. (2) provide four equations for the three unknown coordinates of each point. Equations (2) can be inverted by least squares to determine the object space coordinates. Dynamic triangulation must be preceded by a static calibration to determine the camera calibration constants, and for the case of fixed cameras, the position coordinates of the cameras. The calibration should use at least three fixed targets that will subsequently be visible in the dynamic experiments. These three points serve to define the object space coordinate system. The points are numbered in some arbitrary fashion. We use Point 1 as an arbitrary origin: $(X_1, Y_1, Z_1) = (0,0,0)$. Point 2 is used to define the X axis: $(X_2, Y_2, Z_2) = (X_2, 0, 0)$. Point 3 is used to define the X,Y plane: $(X_3, Y_3, Z_3) = (X_3, Y_3, 0)$. Thus the first three points have a total of three unknowns (X_2, X_3, Y_3), and each additional point introduces three unknowns (X_i, Y_i, Z_i) for a total of 3N - 6 unknown object space coordinates. Notice that each object space point has four associated measurements (two measured coordinates in each of the two image planes). Thus, in the most general case, we have the 3N - 6 unknown object space coordinates plus the 18 unknowns associated with the cameras $(X_{c_i}, Y_{c_i}, Z_{c_i}; \phi_i, \theta_i, \psi_i; x_{o_i}, y_{o_i}, f_i;$ for i = 1,2). We conclude that we have a total of 4N eqns. and 3N + 12 unknowns; if N > 12 conjugate images are measured, we have enough equations to determine all of the 3N object space coordinates and the 18 camera position, orientation, and calibration parameters.

Also of significance, when using Charged Coupled Device (CCD) focal plane arrays (as in the present application), the effective focal length is different for the x and y axes (actually, there is a ratio of the x and y dimensions of the array as a consequence of the rectangular pixels, which can be absorbed into effective focal lengths to be determined during calibration) thereby increasing the number of unknowns by one for each camera and one additional object space point is required. We have found this calibration process to be very well behaved and can be routinely accomplished in 15 minutes of real time.

The calibration process is strengthened, of course, by making redundant measurements and using other a priori measurements of object space points and/or camera calibration parameters. The precision of the results is dependent most heavily upon the accuracy with which the image coordinates are measured and, of course, the geometric strength of the triangulation process. Upon completing a satisfactory static calibration, the subsequent dynamic triangulation process need consider only four of eqs. (2) at a time to sequentially accomplish the least-squares solution for the object space coordinates (X_i, Y_i, Z_i) of the points imaged on the flexible structure.

The major hardware elements are sketched below and described briefly in the table.

Stereo Triangulation Geometry

Major Hardware Elements
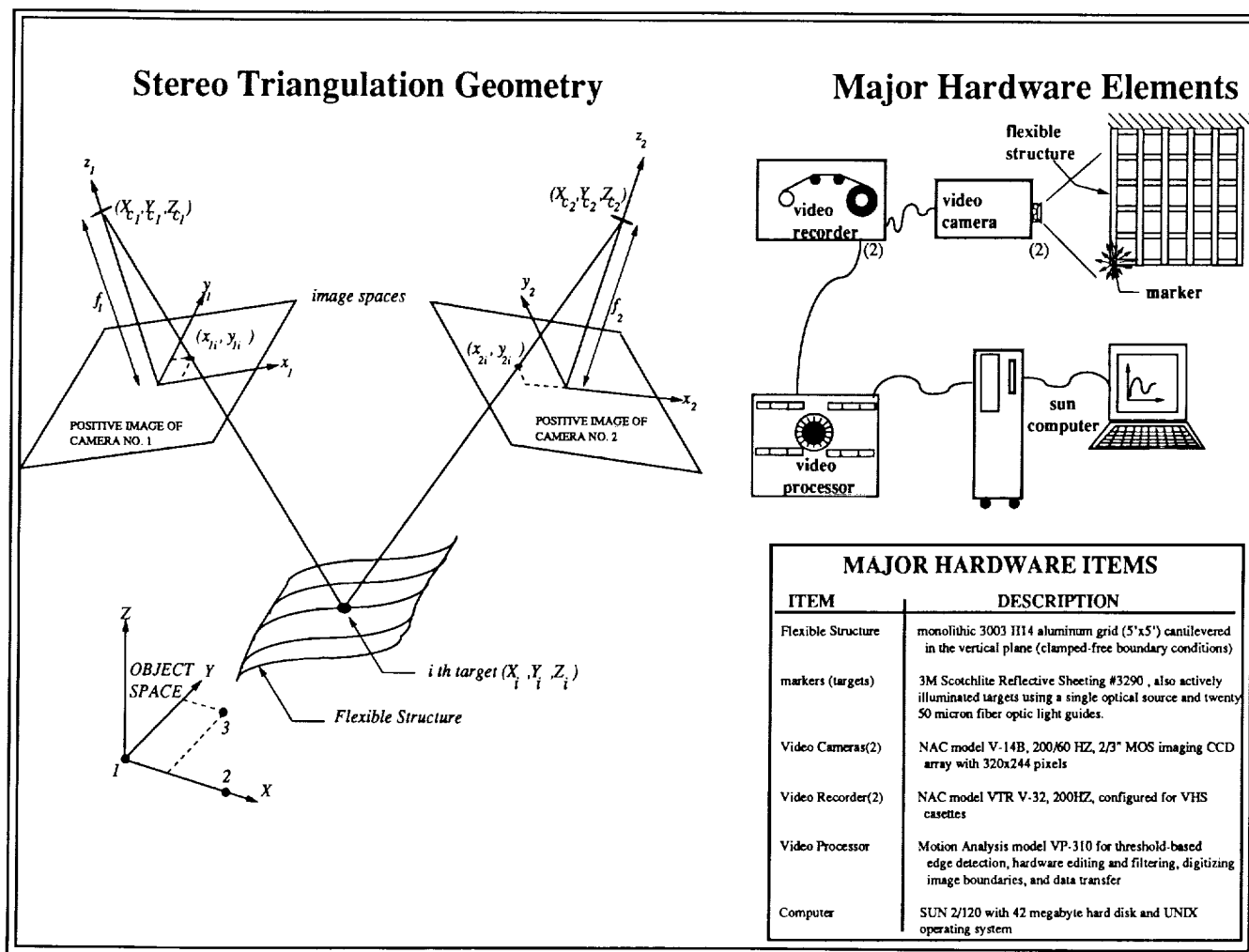
MAJOR HARDWARE ITEMS

| ITEM	DESCRIPTION
Flexible Structure	monolithic 3003 III4 aluminum grid (5'x5') cantilevered in the vertical plane (clamped-free boundary conditions)
markers (targets)	3M Scotchlite Reflective Sheeting #3290 , also actively illuminated targets using a single optical source and twenty 50 micron fiber optic light guides.
Video Cameras(2)	NAC model V-14B, 200/60 HZ, 2/3" MOS imaging CCD array with 320x244 pixels
Video Recorder(2)	NAC model VTR V-32, 200HZ, configured for VHS casettes
Video Processor	Motion Analysis model VP-310 for threshold-based edge detection, hardware editing and filtering, digitizing image boundaries, and data transfer
Computer	SUN 2/120 with 42 megabyte hard disk and UNIX operating system

Here we show two typical measured strain histories at two stations in response
to impulsive excitation via the impulse hammer. The time span of these records is
2.5 seconds; the sample rate was 700 Hz. An initial impulse was applied at the lower
left corner of the grid. Notice from the fast Fourier transform (FFT) of strain
gauge #4 that the response is dominated by the first two modes, but significant exci-
tation was imparted to most of the modes below 40 Hz. On the other hand, strain
gauge #1 has a large contribution by modes 3 and 4. This is not surprising, because
it is intuitively clear that the first torsion mode (mode 2, with nominally zero
strain in the center member) even though excited has near zero strain at station #1,
but the second cantilever mode (mode 3) and the first "bow" mode (mode 4) are heavily
excited by an impulse at the lower left corner, and these modes have significant
strain at station #1. Based upon these and similar experiments, we conclude that the
strain gauges provide excellent sensitivity to all modes below 50 Hz, for impulsive
excitation, and simultaneously using strain measurements at the six stations shown
provide excellent observability for all modes below 40 Hz.

As evident in the next figure, however, we have encountered some signal-to-
noise difficulties when using the strain gauges to measure response to the
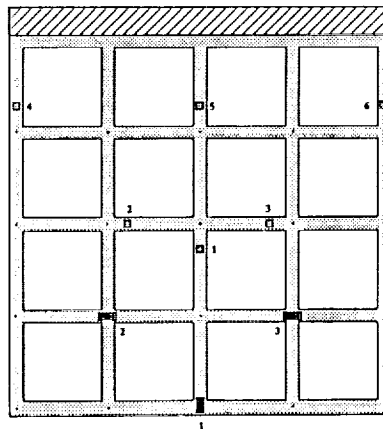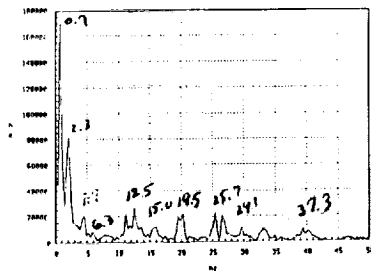reaction wheel excitation.

Response of the Grid to Impulsive Excitation

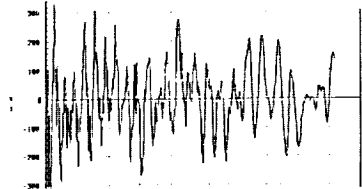**Strain Gauge # 4 Response:**
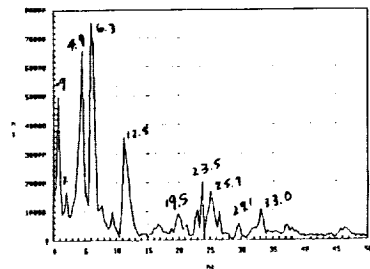Time response history:
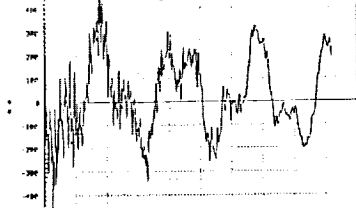
FFT of measured strain history:

Strain Gauge # 1 Response:
Time response history:

FFT of measured strain history:

[calibrated initial impulse applied at lower left corner of the grid]

Below we show two typical measured strain histories at two stations in response to harmonic excitation by reaction wheel #1. A 2-Hz harmonic torque is applied to the structure at the center of the bottom member, about a nominally vertical axis. The torque was applied for approximately 2 minutes to allow a steady state to be achieved before we acquired the above 2.5 seconds of data.

Our experiments indicated that the Clifton Precision motors deliver very clean harmonic excitation, so the high-frequency variations evident in the strain-gauge response are virtually all due to noise. Strain gauge #4 gives data with a satisfactory signal-to-noise ratio. It is evident however that the much smaller strain levels and their closer proximity to the electrical disturbance of the actuator resulted in much noisier data from strain gauge #1. In both cases, the physically dominant steady-state response at 2.0 Hz obviously dominates the strain measurements. However, it is obvious that the "noise modes" are almost negligible in strain gauge #4, whereas they are very significant in strain gauge #1 output. Note the cluster at 60 Hz in the FFT of strain gauge #1's response. This is a near-certain indication that electrical noise from the motor is generating a significant part of the problem. We anticipate that better grounding of the motor will reduce this noise source, but there is the difficulty that locally small strains (which are associated with certain motions) are the fundamental cause of the poor signal-to-noise ratio when using strain gauges as distributed vibration sensors.

These data indicate that the strain gauge is potentially useful in the present application, but other sensing approaches should be explored to eliminate signal-to-noise difficulties. As is evident from the impulsive response in the figure below, the optical sensing methods yield very clean deflection measurements of the low-frequency vibration (<20 Hz), and are therefore very well suited to the present application. We also show below a typical accelerometer record and its FFT. We have found the accelerometer data accurate between 2 Hz and 100 Hz, but very poor below 1 Hz. Our present optical system and triangulation deflection measurements are not compatible with real time. Thus the optical system as we have it presently configured and implemented is suitable for system identification but not feedback control measurements.
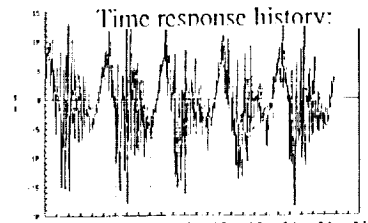
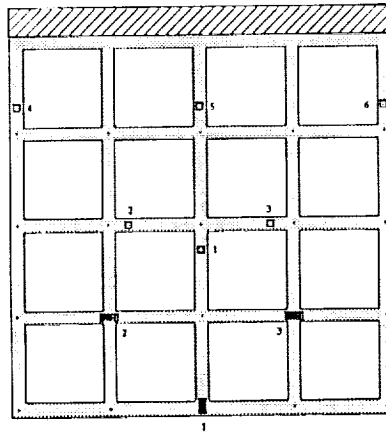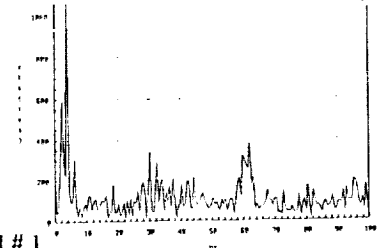# Response of the Grid to Harmonic Excitation

Strain Gauge # 4 Response:

Time response history:

Strain Gauge # 1 Response:
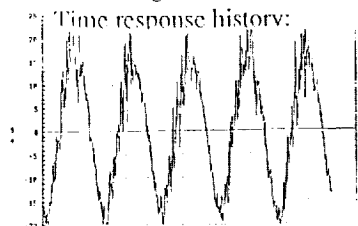
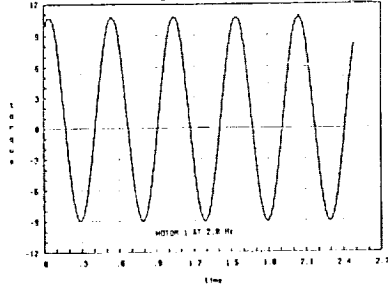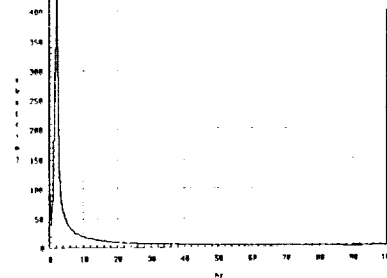Time response history:
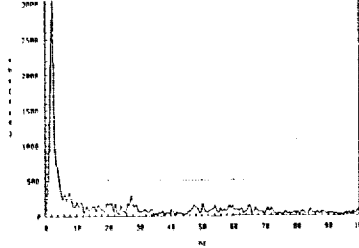
FFT of measured strain history:

FFT of measured strain history:

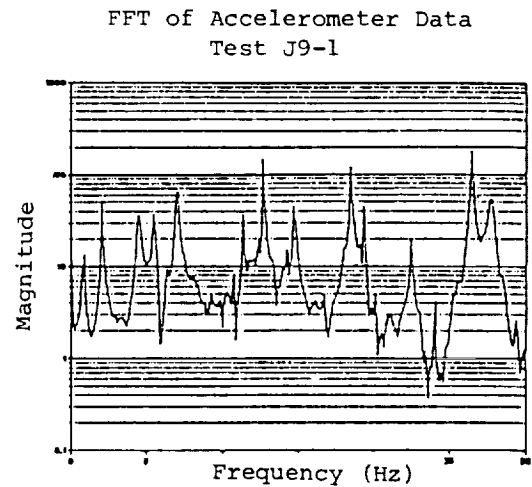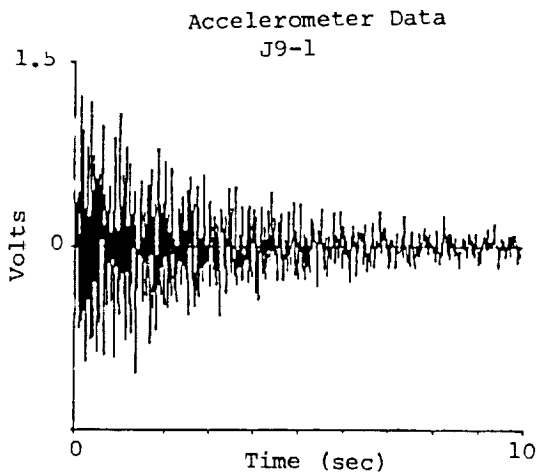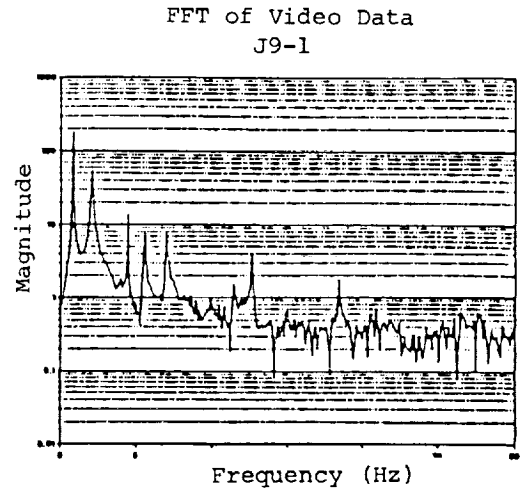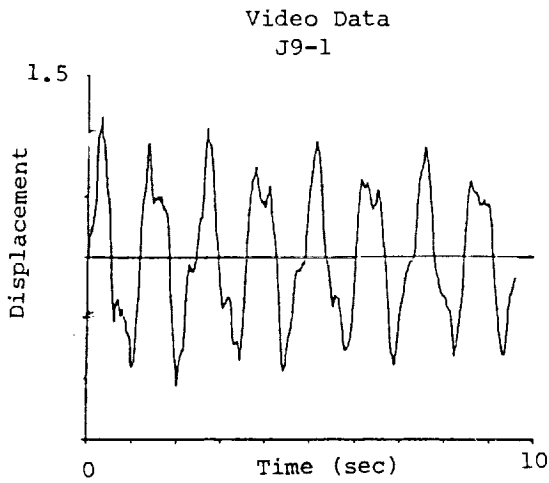**Harmonic Excitation Torque by Reaction Wheel # 1**

Time history of excitation torque

FFT of excitation torque

Comparison of Video-Derived Position
Measurements with Accelerometer Measurements

Video Data
J9-1

Accelerometer Data
J9-1

FFT of Video Data
J9-1

FFT of Accelerometer Data
Test J9-1

The graphs shown above provide some insight into the advantages and disadvantages of the camera system versus an accelerometer. The video data is very useful at the low frequency large amplitude end of the spectrum. The accelerometer response is most reliable at the high frequency end of the spectrum. This data was taken on the AFAL structural identification test article which is similar to the TAMU structure. The video data was taken with a TAMU RCA TC2811 60 Hz video camera. An AFAL Endevco model 7751-500 accelerometer was also used.

Our structural identification approach is based upon the following observations:

- The input/output behavior is uniquely captured by the system transfer function (or frequency response function) matrix, whereas an infinity of structural models has the same transfer function.

- The most important necessary condition of a good model (for control purposes) is that we accurately model the actual system's frequency response over the frequency range of interest.

- Of all the models (realizations) we might use, the most comfortable approach is to modify in some "intelligent" way the model that grew out of our modeling effort (e.g., a finite-element model of the structure).

It is desirable that both free response and forced response behavior be accurately captured by the identified model.

Basic System Realization Concepts

Linear Autonomous System
$$\dot{x} = Ax + Bu$$
$$y = Cx$$

Time Response
$$x(t) = e^{At} x(t_0)t + \int_{t_0}^{t} e^{A(t-\tau)} Bu(\tau)d\tau$$
$$y(t) = C e^{At} x(t_0)t + \int_{t_0}^{t} Ce^{A(t-\tau)} Bu(\tau)d\tau$$

Laplace Transform
$$x(s) = (sI - A)^{-1} Bu(s)$$
$$y(s) = Cx(s) = C(sI - A)^{-1} Bu(s)$$
$$y(s) = G(s) u(s)$$

Transfer Function
$$G(s) = C(sI - A)^{-1} B$$

Freq. Response Function
$$G(j\omega) = C(j\omega I - A)^{-1} B$$

Notes

The triple (A,B,C) is not unique.

But $G(s)$ is unique.

(A_1,B_1,C_1) and (A_2,B_2,C_2) are said to be **equivalent** if any of the following statements are true:
- The transfer functions are equal:
  $$G_1(s) = G_2(s), \text{ for all } s$$
- The weighting patterns are the same:
  $$C_1 e^{A_1 t} B_1 = C_2 e^{A_2 t} B_2$$
- $C_1 A_1^k B_1 = C_2 A_2^k B_2$, for all k.

$\Rightarrow$ **Any** (A,B,C) which produces the correct transfer function $G(s) = C(sI - A)^{-1} B$ is said to be a "realization" of the system.

Consider the case that a force or moment is applied at a point, but the response at many measurement stations is available. For this case, B and therefore $G(j\omega)$ are vectors. Suppose that the frequency response function (vector) is measured over a frequency range $\{\omega_{min} < \omega < \omega_{max}\}$ at the frequencies $\{\omega_1, \omega_2, ..., \omega_m\}$. Use the notation:

$$\tilde{G} = \begin{Bmatrix} \tilde{G}(\omega_1) \\ : \\ \tilde{G}(\omega_m) \end{Bmatrix} = measured \text{ FRF}, \quad G(p) = \begin{Bmatrix} G(\omega_1, p) \\ : \\ G(\omega_m, p) \end{Bmatrix} = computed \text{ FRF using model vector } p$$

(3)

and

$$\tilde{\Omega} = \{\tilde{\Omega}_1 \ \tilde{\Omega}_2 ... \}^T = measured \text{ free vibration } \Omega\text{'s}, \quad \Omega(p) = \{\Omega_1 \ \Omega_2 ...\}^T = computed \ \Omega\text{'s using } p.$$

(4)

We seek the optimal estimate of the model parameter vector p which minimizes

$$J = \frac{1}{2} \int_{\omega_{min}}^{\omega_{max}} \Delta G^T(p,\omega) W_G(\omega) \Delta G(p,\omega) \, d\omega \ + \frac{1}{2} \Delta\Omega^T W_\Omega \Delta\Omega \ , \quad \Delta G(p,\omega) \equiv \tilde{G}(\omega) - G(\omega, p), \quad \Delta\Omega \equiv \tilde{\Omega} - \Omega(p)$$

(5)

For FRF measurements available at discrete frequencies, the integral can be replaced by a discrete summation; we seek to minimize a weighted sum square of the residuals between all measured and modeled FRF's and Ω's:

$$\Delta G \equiv \begin{Bmatrix} \tilde{G}(\omega_1) - G(\omega_1, p) \\ : \\ \tilde{G}(\omega_m) - G(\omega_m, p) \end{Bmatrix} = \text{FRF residuals}, \quad \Delta\Omega \equiv \begin{Bmatrix} \tilde{\Omega}_1 - \Omega_1(p) \\ \tilde{\Omega}_2 - \Omega_2(p) \\ : \end{Bmatrix} = \text{free vib. frequency residuals}$$

(6)

and we are led to the least-squares differential correction algorithm:

$$\begin{Bmatrix} \Delta G \\ \Delta\Omega \end{Bmatrix} = A \Delta p + ... \implies \Delta p = A^\dagger \begin{Bmatrix} \Delta G \\ \Delta\Omega \end{Bmatrix}. \text{ where } A \equiv \begin{bmatrix} \frac{\partial G}{\partial p} \\ \frac{\partial\Omega}{\partial p} \end{bmatrix}, \text{ and } p_{new} = p_{old} + \Delta p$$

(7)

Potential trouble. This approach works great, but only if: (i) the model is "good" and (ii) p_{start} is "close" to p.

Creamer's Three Step Identification Process

Step 1: Identify a subset of the measured frequencies and mode shapes which correlate well with the corresponding modeled frequencies and mode shapes, do a least square correction correction of the stiffness parameterization to improve correlation if necessary.

Step 2: Find the normalization of the eigenvectors (mode shapes) which results in the best least square fit for the FRF, i. e., find $\{a_0, a_1, a_2, \ldots a_{m+1}\}$ to minimize

$$\int_{\omega_{min}}^{\omega_{max}} \left(\tilde{H}_{pq}(j\omega) - H_{pq_{model}}(j\omega)\right)^2 d\omega \ , \quad or \quad \sum_{\omega_{min}}^{\omega_{max}}\left(\tilde{H}_{pq}(j\omega_k) - H_{pq_{model}}(j\omega_k)\right)^2$$

where

$$H_{pq_{model}}(j\omega) = \frac{a_0}{\omega^2} + \sum_{r=1}^{m} \frac{\tilde{\phi}_{pr}\tilde{\phi}_{qr}}{\tilde{\omega}_r^2 - \omega^2} a_r + a_{m+1}$$

Step 3: Estimate values for the linear mass and stiffness parameterization to satisfy the orthonormality conditions in a least square sense; this leads to the following pair of linear equations for μ_r, *and* κ_r *in* $M = M_o + \Sigma_i \, \mu_i M_i$, $K = K_o + \Sigma_i \, \kappa_i K_i$:

Here we show the first five free vibration mode shapes. In the table, we list
the a priori finite-element model prediction of the first five natural frequencies,
the values recovered from using the Eigenstructure Realization Algorithm to reduce an
impulse response of the grid as measured by the stereo triangulation process. As is
evident, the agreement is generally good with the most significant prediction errors
in the higher modes as might be expected. Applying substructure scale factors to the
members contribution to the mass and stiffness matrices resulted in an identified
structure with near-identical measured and modeled natural frequencies and mode
shapes. The measured modes differed most significantly in that the first mode was
observed to have a slight degree of torsion whereas the modeled first mode was a pure
cantilever mode. The discrepancy was traced to a slight bend near the upper right of
the structure, apparently this occurred when the structure was being mounted.

Using only the optical data, we have demonstrated that the free response and
input/output behavior of this structure can be accurately identified using the stereo
triangulation system and the methodology we have developed. The presently imple-
mented system works well only for frequencies below approximately 15 Hz. The dif-
ficulty at higher frequencies is not a consequence of the camera frame speed
(200 frames/sec), but rather because the limited spatial resolution of our cameras
cannot "see" the small amplitude vibrations associated with the higher modes.

Modeled, Measured and Identified Modes of the Grid
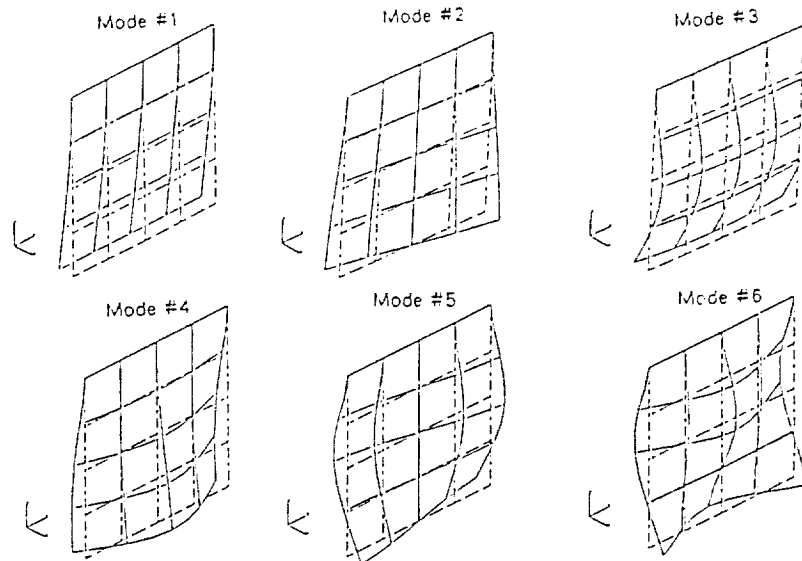
Mode No.	Modeled Value	Measured Value	Identified Value
1	.90 Hz	.92 Hz	.91 Hz
2	2.34	2.32	2.32
3	4.85	4.93	4.93
4	6.05	6.38	6.38
5	7.78	7.27	7.26

377

The appendage/hub structure was designed, fabricated, and assembled so as to produce a structure that is symmetric with respect to physical and geometric parameters and that is also subject to a minimal dynamic asymmetry. Phasing problems that exist between appendages are apparent only after free vibrations are allowed to continue for several minutes. This permits free and forced vibration data to be recorded for a structure that exhibits an initial dynamic symmetry.

TAMU Maneuver and Vibration Suppression Experiment
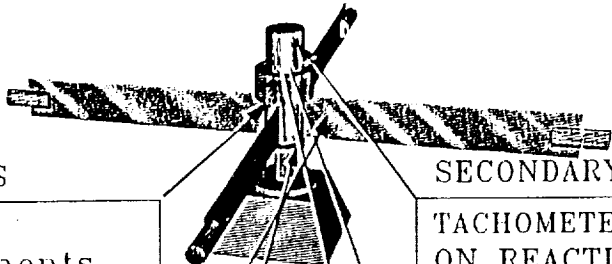
PRIMARY SENSORS

TORQUE SENSOR
Sensor Developments
custom unit   with
signal conditioner

STRAIN GAGES

Micromeasurements Div.
Measurements Group
Std. metal film

ANGLE ENCODER
Teledyne Gurley 8708
36000 counts / rev
C-TEK counter
mod. LIN-101-5021418E

SECONDARY SENSORS

TACHOMETER
ON REACTION WHEEL
PMI Motion Technologies

MOTOR CURRENT MONITOR

hard wired to
A/D board

MOTOR VOLTAGE MONITOR

hard wired to
A/D board

The below maneuver is from a student (Robert Byers') recent M. S. thesis (ref. 3). Byers implemented a variable-structure feedback control law that roughly approximates a smoothed bang-bang near-minimum-time maneuver, but also exhibits good vibration suppression characteristics as is evident. The variable-structure approach is one of several robust control concepts we have studied in recent months, and we are engaged in an experimental effort to parallel and support our analytical activities.

As an alternative approach, we show below an output feedback control law that is based upon a PDE description of the system dynamics, and we prove global stability using Lyapunov's second method. This method is found to be very robust and, since it does not require a state estimator and since no spatial discretization approximations are introduced, it does not suffer from spillover; we feel this is a very attractive approach. We have shown that a near-minimum-time torque-shaped open-loop maneuver can be introduced and the Liapunov based method leads to a tracking-type feedback control that is theoretically globally stable and is, in fact, very robust with respect to modeling and implementation errors. It is this latter idea upon which we have based our early experiments; we will therefore go over the key ideas underlying this approach.
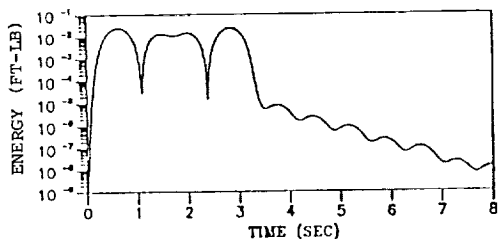
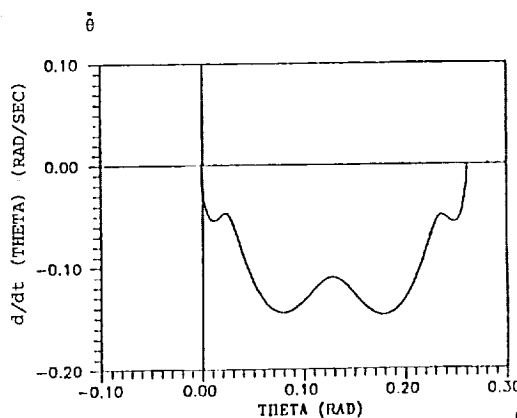# Texas A&M Maneuverable Space Structure Experiment

15° Rest-to-Rest Maneuver
$$T_1 = .35 \text{ sec}, \alpha = .93, \beta = .97, \psi = \varphi = 0$$
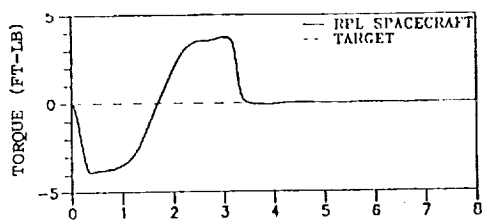
(a) control profile, (b) flexible mode energy,
(c) state space trajectory

The below figure shows a torque-shaped, near-minimum-time control for the
flexible hub derived using the methods of Roger Thompson et al. (ref. 6). This
maneuver served as a nominal open-loop control. We used a generalization of the
Liapunov control approach to develop a tracking like a globally stable feedback
control law to null errors in the event of non-nominal initial conditions, model er-
rors, and control implementation errors. The open-loop maneuver is designed in such
a fashion that the maneuver time is about 20-percent longer than a strict bang-bang
maneuver of a rigid structure having the same undeformed inertia. However the
residual energy of vibration (without feedback) of the flexible structure is theo-
retically reduced by about 5 orders of magnitude by using the torque-shaped maneuver
in lieu of a bang-bang profile. Thus the open-loop control is designed to incur
small vibrations during and upon completion of the maneuver, and the feedback control
is designed to suppress residual vibrations which arise from whatever physical
origin.

A Torque-Shaped Near-Minimum Time Maneuver of the TAMU Fexible Structure

(Test Run No. 3 of 01/25/89)

u
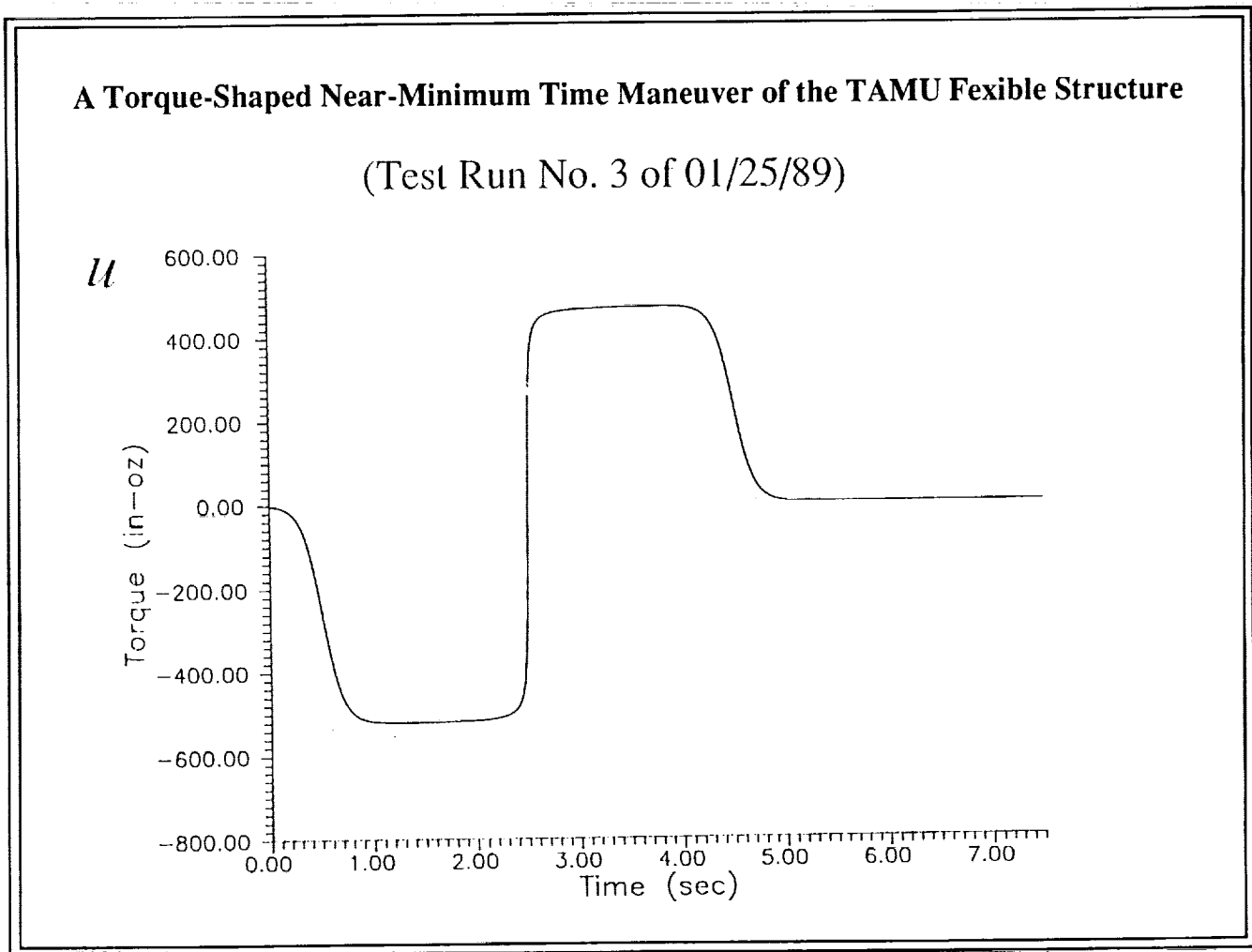
The below figure shows the experimentally achieved hub rotation angle as a function of time for a 40° near-minimum time maneuver. The first half of the maneuver was almost identical to the corresponding simulation (slight lag developed due to a lag in the compensator circuit of our power supply). However a large transient occurred at precisely the instant (maneuver mid-point) the commanded current reversed to initiate the breaking phase of the maneuver. This is because our low-budget power supply was unable to accurately generate the commanded current in the face of the variable load presented by the motor near torque reversal. During the last half of the maneuver, the power supply compensation circuits and control commands combined to arrest rotation and vibration with a moderate overshoot.

While the problems with our power supply are evident, we feel pleased with this first implementation of our approach and anticipate substantially improved results in future experiments.

A Large Angle Maneuver of the TAMU Flexible Structure
(Test Run No. 3 of 01/25/89)
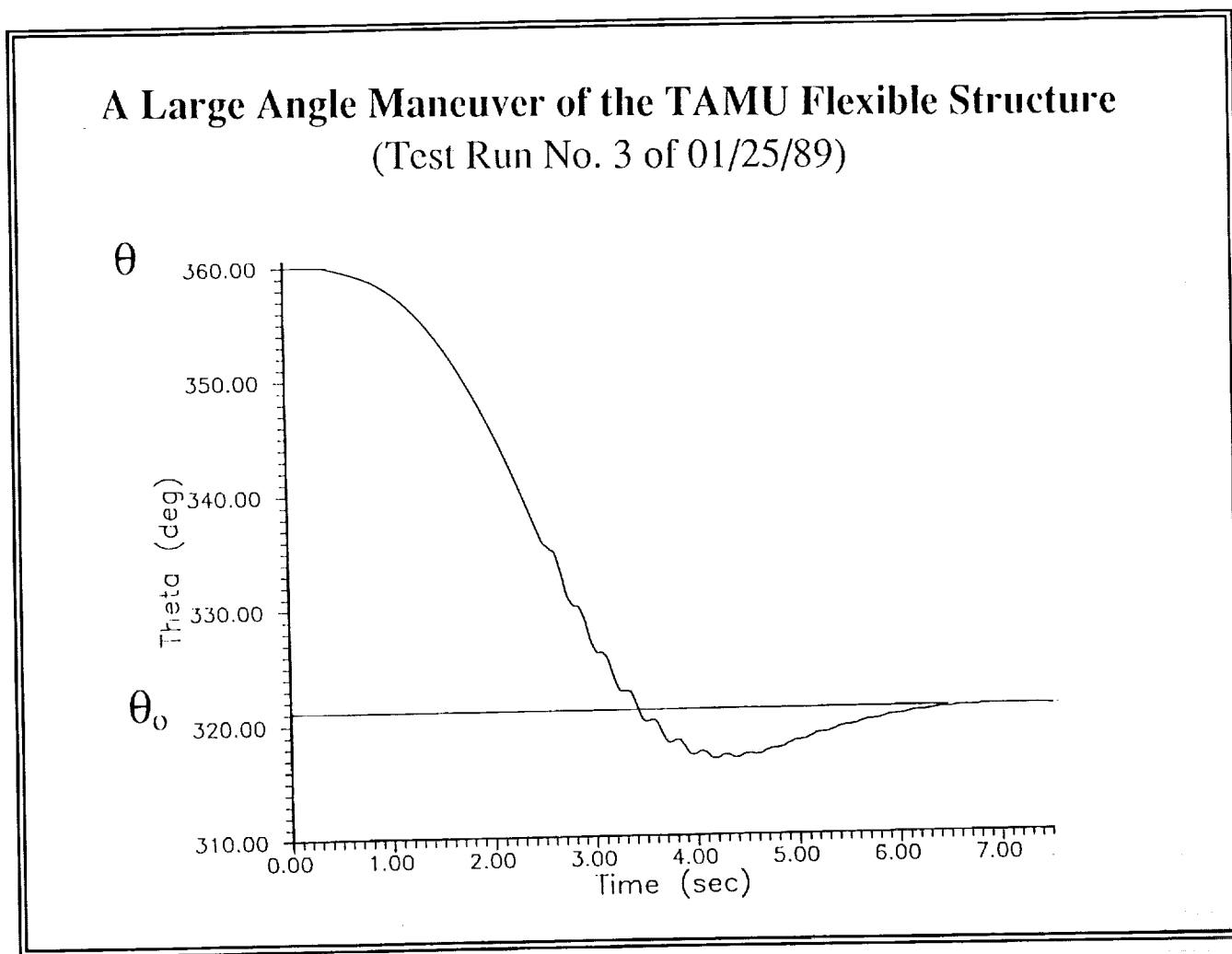
Concluding Remarks

- Novel Vibration Sensing and System Identification Methods have been Developed and Demonstrated

- Large Angle, Near-Minimum-Time, Feedback Control for Flexible Body Maneuvers have been Developed and Successfully Demonstrated

- Both of the Above are in a Preliminary State of Development, but Our Results to Date are Significant

384

References

1. Creamer, N. G. and Junkins, J. L., Identification Method for Lightly Damped Situations. AIAA Journal of Guidance, Control, and Dynamics, vol. 11, no. 6, Nov.-Dec. 1988, pp. 571-576.

2. Manual of Photogrammetry, Chapter 17, 4th ed., published by the American Society of Photogrammetry, Falls Church, VA, 1980.

3. Byers, R. M., Feedback Control for Smooth, Near-Minimum Time Rotational Maneuvers of Flexible Spacecraft, MS Thesis, Texas A&M University, Department of Aerospace Engineering, August 1987.

4. Fujii, H., Ohtauka T., and Udou, S., Mission Function Control for Slew Maneuver Experiments, AIAA J. of Guidance, Control, and Dynamics, 1989.

5. Rahman, Z., Junkins, J. L., Pollock, T. C., and Bang, H., Large Angle Maneuvers with Vibration Suppression: Analytical and Experimental Results, Paper presented at 7th VPI and SU Symposium on Dynamics and Control of Large Structures, May 1989.

6. Thompson, R. C., Junkins, J. L., and Vadali, S. R.: Near-Minimum Time Open-Loop Slewing of Flexible Vehicles, AIAA Journal of Guidance, Control, and Dynamics, vol. 12, no. 1, Jan.-Feb. 1989, pp. 82-88.